Measurement of fracture aperture fields using transmitted light: An evaluation of measurement errors and their influence on simulations of flow and transport through a single fracture

Russell L. Detwiler

Department of Civil, Environmental, and Architectural Engineering, University of Colorado, Boulder

Scott E. Pringle and Robert J. Glass

Flow Visualization and Processes Laboratory, Sandia National Laboratories, Albuquerque, New Mexico

Abstract. Understanding of single-phase and multiphase flow and transport in fractures can be greatly enhanced through experimentation in transparent systems (analogs or replicas) where light transmission techniques yield quantitative measurements of aperture, solute concentration, and phase saturation fields. Here we quantify aperture field measurement error and demonstrate the influence of this error on the results of flow and transport simulations (hypothesized experimental results) through saturated and partially saturated fractures. We find that precision and accuracy can be balanced to greatly improve the technique and present a measurement protocol to obtain a minimum error field. Simulation results show an increased sensitivity to error as we move from flow to transport and from saturated to partially saturated conditions. Significant sensitivity under partially saturated conditions results in differences in channeling and multiple-peaked breakthrough curves. These results emphasize the critical importance of defining and minimizing error for studies of flow and transport in single fractures.

1. Introduction

Flow and transport through fractures and fracture networks in the subsurface has become an important area of study in contaminant hydrology. Understanding of the fundamental building block, the single fracture, has been stunted owing to the difficulties of testing theory with experiment. It is extremely difficult to measure the void geometry of single fractures in rock at sufficient resolution to thoroughly test current hypothesized models of flow and transport processes. Recently, however, rough-walled transparent fractures have been used to study a variety of two-phase flow processes [e.g., *Nicholl et al.*, 1992; *Glass and Nicholl*, 1995; *Kneafsey and Pruess*, 1998; *Su et al.*, 1998; *Geller et al.*, 1998]. In transparent systems, quantitative experimental studies of single-phase and multiphase flow and transport in fractures can be conducted by applying light transmission techniques to measure both aperture and critical state variable fields (e.g., phase occupancy and dye tracer concentration) as a function of time with high spatial and temporal resolution. Transparent fractures can be designed and fabricated to systematically vary aperture through a range of probable structures or cast from individual natural fractures in epoxy [e.g., *Gentier et al.*, 1989; *Hakami and Barton*, 1991; *Persoff and Pruess*, 1995] or glass (J. Wan et al., Glass casts of rock fracture surfaces: A new tool for studying flow and transport, submitted to *Water Resources Research*, 1999) (hereinafter referred to as Wan et al., submitted manuscript, 1999) to yield single realizations of nature. This approach allows the aperture field to be easily measured over the entire fracture at the time of an experiment, thus eliminating errors due to cell

assembly that often limit reproducibility and subsequent data interpretation.

While light transmission methods for measuring aperture fields have been applied previously [e.g., *Glass and Nicholl*, 1995; *Persoff and Pruess*, 1995; *Brown et al.*, 1998], they have not been thoroughly evaluated with respect to error and therefore yield data of ambiguous quality. Additionally, the influence of this error on our interpretation of the underlying physics within a particular single-phase or multiphase experiment has yet to be considered. The appropriate design of experiments required to advance our understanding of the fundamental physics demands that both of these evaluations be accomplished. In this paper, we evaluate aperture field measurement error for the light transmission technique, outline a measurement protocol to obtain a minimum error field (optimal field), and demonstrate the influence of accuracy on hypothesized experimental results using simulations of flow and transport through saturated and partially saturated fractures.

To enhance our understanding of the light transmission technique, we independently evaluate each source of error that contributes to the total measurement error. We find reducing measurement error requires balancing precision (random error) and accuracy (systematic or bias error) to minimize the total error for a particular fracture and light transmission apparatus. With this understanding we formulate a general protocol for measuring aperture fields. For our system, measurements on a representative "baseline" rough-walled fracture yielded an estimated root-mean-square (RMS) error of 0.9% (0.002 mm) of the mean aperture (0.222 mm) across the entire field of $\sim 2 \times 10^6$ points with a spatial resolution of 0.159 × 0.159 mm. Other imaging techniques applied to fractures in rock cores, such as X-ray computed tomography [e.g., *Johns et al.*, 1993] and nuclear magnetic resonance [e.g., *Kumar et al.*,

1995], also allow the aperture field to be measured at the same time as flow and transport experiments are conducted; however, the reported measurement errors are significantly larger (~10% of the mean aperture), the spatial resolution is lower (~ an order of magnitude), and the size of the data set is much smaller (~2–3 orders of magnitude).

To demonstrate how aperture measurement error can influence our interpretation of experimental results and thus our ability to test various conceptual models that presumably embody the underlying physics, we compared simulations of flow and transport in an optimal aperture field to simulations in two fields generated using earlier, nonoptimal approaches that artificially narrowed and widened the aperture distribution (estimated RMS errors of 4.8 and 12.2%, respectively). Under saturated conditions we find fracture transmissivity relative to the optimal field to be minimally affected (~103–92%), while for dispersivity, sensitivity was greatly enhanced (~85 to 330%). For partially saturated conditions where a modified invasion percolation model defined a residual entrapped nonwetting fluid (e.g., air or an organic liquid) around which flow occurs, deviations were compounded with ranges in transmissivity relative to the optimal of ~167–85% and transport simulations that demonstrate significant qualitative and quantitative differences in the nature of channeling and resultant multiple-peaked breakthrough curves.

Obviously, the experimental characterization of aperture field error is extremely important when we design experiments to test hypothesized conceptual models for flow and transport in fractures. In transparent systems we can obtain rapid measurements of fracture aperture fields with low, quantifiable error that can be combined easily with solute concentration and phase occupancy fields to make an ideal tool for studying the physics of flow and transport.

2. Application of Light Absorption Theory to the Measurement of Aperture Fields

For a monochromatic light source the Beer-Lambert law describes transmitted light intensity I through a light-absorbing solute (dye) as

$$I = I_o e^{-\mu Cd + \xi} \tag{1}$$

where I_o is the incident light intensity, μ is the absorptivity of the solute, C is solute concentration, d is the gap width filled with absorbing solute, and ξ is a constant that accounts for absorbance by the solvent and the apparatus containing the solute [e.g., *Rossiter and Baetzold*, 1993, pp. 16–17]. For two different solute concentrations $(C_1$ and $C_2)$, assuming I_o is constant, (1) can be rewritten as

$$\ln (I_1/I_2) = \mu(C_2 - C_1)d = A \tag{2}$$

where absorbance A of the solute is a linear function of concentration.

We measure the light intensity transmitted through a transparent fracture, I_{ij} (where i and j represent the location of each measurement within the field), simultaneously at an array of points using a charge-coupled device (CCD) camera. From (2) and knowledge of μ, sequential filling of the fracture with two solutions of different dye concentrations yields the fracture aperture field d_{ij}. As CCD response is inherently linear [*Russ*, 1992], it is not necessary for $I_{o_{ij}}$ to be uniform over the entire field; however, $I_{o_{ij}}$ must be constant in time at location ij of the field.

Assuming μ, C_1, and C_2 are constant throughout the entire field, setting C_1 to zero, C_2 to C, and averaging (2) over the field yields

$$\langle A_{ij} \rangle = \langle \ln (I_{cl_{ij}}/I_{dye_{ij}}) \rangle = \mu C \langle d_{ij} \rangle \tag{3}$$

where $\langle \ \rangle$ indicates spatial averaging over all ij and $I_{cl_{ij}}$ and $I_{dye_{ij}}$ are the intensities at location ij of the clear $(C_1 = 0)$ and dyed $(C_2 = C)$ fields, respectively. Combining (2) and (3) gives

$$d_{norm_{ij}} = d_{ij}/\langle d_{ij} \rangle = A_{ij}/\langle A_{ij} \rangle \tag{4}$$

As first proposed by *Glass et al.* [1991], we can obtain d_{ij} without measuring μ if we independently measure the mean aperture d_{avg}. Multiplying $d_{norm_{ij}}$ by an independently measured d_{avg} yields the dimensional aperture field d_{ij}. In application, the choice of measuring either μ or d_{avg} must be made. We recommend direct measurement of d_{avg} as it critically controls flow and transport in fractures and is easily accomplished (see section 4.1).

3. Measurement System

The measurement system includes a rotating test stand, diffuse light source, transparent fracture cell, and charge-coupled device (CCD) camera (Figure 1a). The design of this system was first introduced by *Glass and Tidwell* [1991] (reprinted version of paper SAND90-3042C contains additional figures) and has been used extensively to study a variety of single-phase and multiphase flow and transport processes in fractures [e.g., *Nicholl et al.*, 1994; *Nicholl and Glass*, 1994; *Glass and Nicholl*, 1995]. Here we discuss each of these components in more detail than was presented in these references. We also include a description of the method used to correct for temporal fluctuations of the light source and an evaluation of temporal and spatial variability of CCD response.
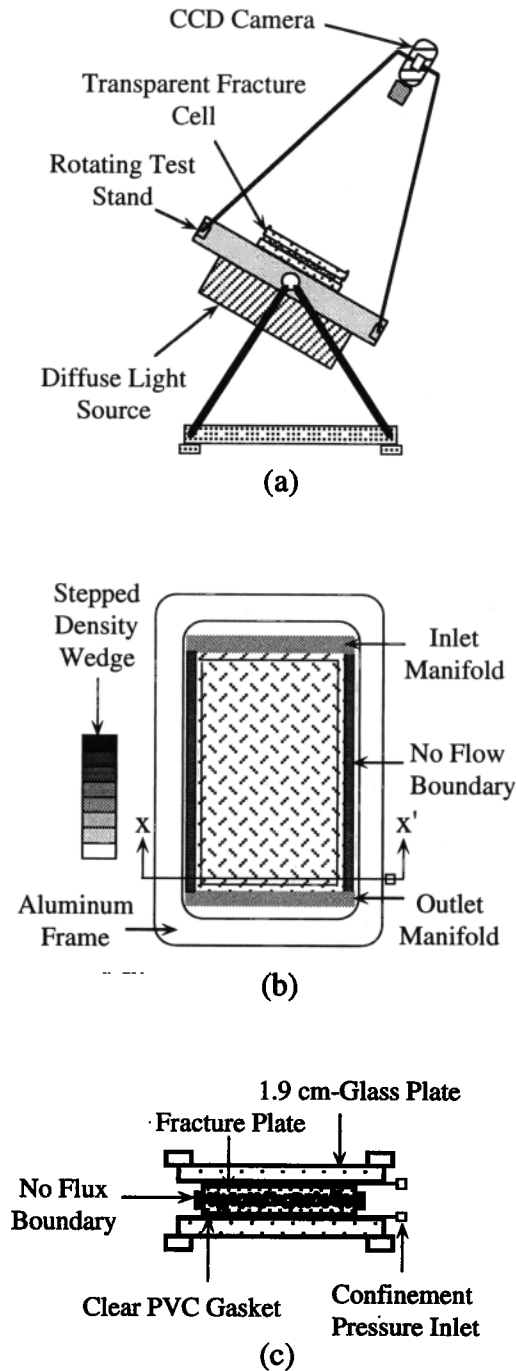
3.1. Test Stand and Fracture Cell

The test stand rigidly connects the light source, fracture cell, and camera to reduce relative movement of any one of the system components with respect to any other component while allowing rotation through 180° so gravitational forces acting on the liquid phase can be varied. As it is impossible to make the stand perfectly rigid, the camera can experience small shifts (typically <1 CCD pixel) relative to the fracture cell. Opaque fabric covers the test stand to prevent external stray light from influencing measurements.

Fracture cells are constructed such that the entire aperture field is measurable. A fracture cell consists of two rectangular aluminum frames each mounted to a 1.9-cm (3/4-inch) thick glass window (Figures 1b and 1c). A fracture plate, which is typically textured glass or epoxy-glass casts of rock fractures, is mounted on the inside of each plate glass window separated by a clear PVC gasket. This configuration results in a small space between the window and the fracture plate that can be pressurized. The cell is assembled by placing the fracture plates in contact and bolting the frames together to a uniform torque (typically 0.085 N m). Compressed air is used to pressurize each side of the fracture to a desired normal force (typically 138 kPa). This confinement pressure controls fluctuations in the aperture field due to varying fluid pressures and reduces long-wavelength variation imposed during fabrication of the glass and assembly of the fracture cell. Constant flux, constant
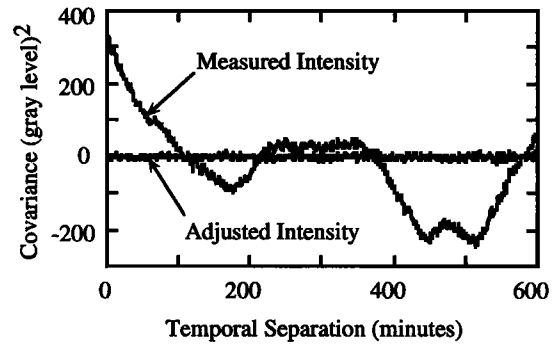
head, or no flux boundaries can be applied to each of the four fracture edges. For the evaluation of our measurement system presented in section 4 we used a representative "baseline" test fracture constructed by mating two 150 × 300 mm textured glass plates.

3.2. Light Source

The light source consists of a three-dimensional array of fluorescent bulbs driven by ballasts at a frequency that is much

Figure 2. Covariance as a function of temporal separation of measured intensity ($I_{\text{meas}_{ij}}$ in equation (5)) and adjusted intensity (I_{ij} in equation (6)) at a single, representative location of the field. The lack of correlation in the adjusted intensities indicates that applying $f^{-1}(I_{\text{meas}_{ij}}, t)$ to $I_{\text{meas}_{ij}}$ is an effective method of removing the influence of temporal fluctuations in the light source from each image.

Figure 1. Schematic of the experimental apparatus showing (a) the major components of the system, (b) plan view of the test cell and stepped density wedge, and (c) cross section X-X' of the test cell.

higher than the relaxation time of the phosphors in the bulbs (no flicker). A photoresistor continuously monitors the output intensity of the bulbs and is part of a feedback circuit that regulates the voltage to the ballasts driving the bulbs, thus maintaining a near-steady output intensity from the light source. Because bulb output is sensitive to temperature, the light source is contained in a box through which fans drive controlled temperature air (±1°C) past the bulbs. A diffuser plate between the fracture cell and the bulbs improves the spatial uniformity of the light source and ensures that light rays crossing the fracture cell at any one point come from many different directions (i.e., diffuse light). A thermopane (with infrared filter) beneath the diffuser plate reduces heat transfer from the light source. The output frequency of the light source can be controlled by the choice of bulbs and by filters placed between the bulbs and the fracture cell.

Because of the nature of feedback circuits and small fluctuations in temperature, some variability in the intensity of the light source is inevitable. As discussed in section 2, using this system to measure fracture aperture requires that the light source intensity $I_{o_{ij}}$ be constant with time. We define the measured light intensity at location ij as

$$I_{\text{meas}_{ij}} = f(I_{\text{meas}_{ij}}, t)I_{ij} \qquad (5)$$

where $I_{\text{meas}_{ij}}$ is the light intensity measured by the camera, $f(I_{\text{meas}_{ij}}, t)$ is a function describing temporal fluctuations in the light source intensity, and I_{ij} is a steady intensity. We monitor temporal fluctuations of $I_{o_{ij}}$ using a stepped density wedge (photographic step tablet) located adjacent to the fracture cell (Figure 1b). The intensities measured at each wedge step allow development of an adjustment function for temporal light intensity fluctuations, $f^{-1}(I_{\text{meas}_{ij}}, t)$, for each image. A plot of the covariance functions of measured and adjusted intensities as a function of separation in time, for a single representative location from a series of images (Figure 2), demonstrates the effectiveness of $f^{-1}(I_{\text{meas}_{ij}}, t)$ at describing and thus removing the influence of temporal fluctuations of the light source. The adjusted values are clearly uncorrelated at even the shortest separation (47 s), while the measured intensities show strong temporal correlation and periodic behavior. This method for removing temporal fluctuations in light source intensity requires that fluctuations detected at the wedge represent fluc-
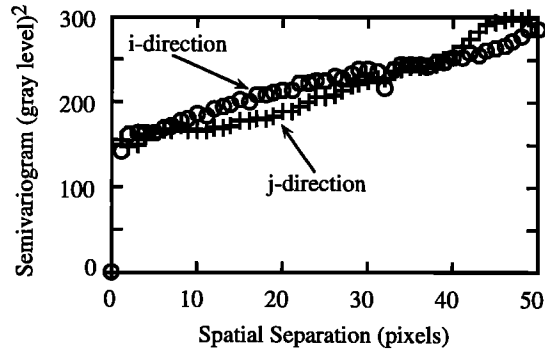
Figure 3. Semivariograms in the i and j directions of charge-coupled device (CCD) response to a near-uniform field. The trends in the semivariograms are due to a spatial trend in the field, while the nugget at ~150 (gray levels)^2 is due to spatial variability of CCD response.

tuations over the entire field. This must be confirmed by comparing multiple full-field images of the light source after adjusting the intensities using (5). Subtracting any two of these fields should result in fields with no spatial correlation.

3.3. CCD Camera

A 12-bit CCD camera (Photometrics with Kodak KAF-4200 Scientific Grade chip) measures the light intensity field transmitted through the fracture cell. The CCD has an array of 2033 × 2048 pixels each with a range of 4096 gray levels. Filters on the camera lens limit the wavelength of light transmitted to the camera to a range optimally absorbed by the chosen dye (e.g., Warner Jenkins FD&C Blue #1 in the current study). For the evaluation of our measurement system described in section 4 we acquired all images with the focal plane ~1.1 m above the fracture plane, resulting in a spatial resolution of 0.159 mm. Exposure times were ~0.7 s with an f-stop of 11. Two filters added to the camera lens (Kodak Red #25 and Kodak Infra Red #301A) decrease the range of wavelengths measured by the camera to those absorbed most effectively by the dye.

CCD response exhibits temporal variability (i.e., noise) at each pixel as well as spatial variability. Because the spatial variability is constant in time, it influences measurements only if there is a camera shift relative to the fracture cell, whereas noise leads to uncertainty in measurements at each pixel in every image. To quantify the influence of temporal and spatial variability on measurements of I_{ij}, we define

$$I_{ij} = E[I_{ij}] + n_{ij} + s(\Delta i, \Delta j)_{ij} \tag{6}$$

where I_{ij} is the light intensity adjusted for light source fluctuations (from (5)), $E[I_{ij}]$ is the expected intensity (i.e., all error removed), n_{ij} is a random error due to CCD signal noise, and $s(\Delta i, \Delta j)$ is a random error in measured intensity caused by spatial variability in CCD response when correcting for a movement of the camera relative to the fracture cell of magnitude Δi, Δj. We then quantify the uncertainty in I_{ij} as the variance of (6):

$$\text{Var}[I_{ij}] = \text{Var}[n_{ij}] + \text{Var}[s(\Delta i, \Delta j)]_{ij} \tag{7}$$

where $\text{Var}[I_{ij}]$ and $\text{Var}[n_{ij}]$ are the temporal variances of I_{ij} and n_{ij} at pixel ij and $\text{Var}[s(\Delta i, \Delta j)]_{ij}$ is the variance measured over the field due to a shift between images of magnitude

Δi, Δj. For a shift of magnitude Δi, Δj at location ij, $s(\Delta i, \Delta j)$ is constant but difficult to quantify; thus we use $\text{Var}[s(\Delta i, \Delta j)]_{ij}$ as a measure of the uncertainty (mean square error) at any location ij. This inherently assumes that the mean over the field of $s(\Delta i, \Delta j)$ is zero. Also, (7) assumes that there is no correlation between n_{ij} and $s(\Delta i, \Delta j)$. This is reasonable since n_{ij} is both random and uncorrelated (see Figure 2), whereas $s(\Delta i, \Delta j)$ is constant for two images displaying the same shift.

For our CCD we measured the relationship between $\text{Var}[n_{ij}]$ and the measured intensity at any location ij to be

$$\text{Var}[n_{ij}] = (0.0523 \pm 0.0001)I_{ij} \tag{8}$$

where the ±0.0001 bounds on the slope are 95% confidence intervals. Because n_{ij} is random and uncorrelated, we can improve the precision of I_{ij}, our estimate of $E[I_{ij}]$, by averaging a series of m images to yield $\bar{I}_{ij}$ with

$$\text{Var}[n_{ij}] \cong 0.0523\bar{I}_{ij}/m \tag{9}$$

To determine $\text{Var}[s(\Delta i, \Delta j)]_{ij}$ for our CCD, we constructed semivariograms of a near-uniform field formed by averaging 4000 images to essentially remove n_{ij} (Figure 3). The semivariograms, in both the i and j directions, have a nugget at ~150 (gray levels)^2 and a trend due to long wavelength variability in the near-uniform field. We use the value of the nugget as an estimate of the variability of CCD response or $\text{Var}[s(\Delta i, \Delta j)]_{ij}$ for Δi or $\Delta j \geq 1$ and assume a straight line approximation of the semivariograms between 0 and 1 to yield

$$\text{Var}[s(\Delta i, \Delta j)]_{ij} \cong 0.0410 \max (\Delta i, \Delta j)\bar{I}_{ij} \tag{10}$$

where $\max(\Delta i, \Delta j)$ equals the maximum value of Δi and Δj when both are less than one pixel and equals one when either is greater than one pixel. Because these errors are correlated between images with the same shift, we cannot reduce $\text{Var}[s(\Delta i, \Delta j)]_{ij}$ by averaging a series of images. Substituting (9) and (10) into (7), for an average of m images, yields an expression for the variance of the average intensity at a location ij,

$$\text{Var}[\bar{I}_{ij}] = (0.0523\bar{I}_{ij}/m) + 0.0410 \max (\Delta i, \Delta j)\bar{I}_{ij} \tag{11}$$

which, as described in detail in section 4.2, can be used to define the contribution of temporal and spatial variability in CCD response to precision error in aperture measurements.

4. Measurement Error Evaluation

As presented in section 2, aperture measurements d_{ij} are made by multiplying the normalized aperture determined using light absorbance theory $(d_{\text{norm}_{ij}})$ and the volumetrically measured dimensional mean aperture d_{avg}. Measurements of both $d_{\text{norm}_{ij}}$ and d_{avg} have associated errors which must be combined to yield the total measurement error. We quantify these different error sources independently and combine them to obtain an estimate of the total mean square error in d_{ij} measured over all ij. A first-order perturbation analysis of $d_{ij} = d_{\text{avg}}d_{\text{norm}_{ij}}$ yields

$$\langle d_{ij}^{\prime 2} \rangle \cong \text{Var}[d_{\text{avg}}] + \langle d_{\text{norm}_{ij}}^{\prime 2} \rangle E[d_{\text{avg}}]^2 \tag{12}$$

where $\langle d_{ij}^{\prime 2} \rangle$ and $\langle d_{\text{norm}_{ij}}^{\prime 2} \rangle$ are the mean square errors (over all ij) of d_{ij} and $d_{\text{norm}_{ij}}$, respectively.

We separate $d_{\text{norm}_{ij}}^{\prime}$ into two fundamental types of errors: precision and accuracy. Precision (or random) errors $e_{p_{ij}}$ are

due to the random variability of intensity measurements caused by random temporal and spatial variability in the CCD response (n_{ij} and $s(\Delta i, \Delta j)$ in section 3.3). Accuracy (or bias) errors $e_{a_{ij}}$ are due to the absorbance and refractive characteristics of the fluid used for measuring aperture and the geometry of the aperture field. We can then define $d'_{\mathrm{norm}_{ij}}$, the total error in $d_{\mathrm{norm}_{ij}}$ at location ij, as

$$d'_{\mathrm{norm}_{ij}} = e_{a_{ij}} + e_{p_{ij}} \qquad (13)$$

Assuming negligible correlation between $e_{p_{ij}}$ and $e_{a_{ij}}$, we describe the mean square error across the field as

$$\langle d'^2_{\mathrm{norm}_{ij}} \rangle = \langle e^2_{p_{ij}} \rangle + \langle e^2_{a_{ij}} \rangle \qquad (14)$$

Thus independently quantifying $\mathrm{Var}[d_{\mathrm{avg}}]$, $\langle e^2_{p_{ij}} \rangle$, and $\langle e^2_{a_{ij}} \rangle$ allows us to use (12) to obtain an estimate of the mean square error in d_{ij}.

In the following sections we quantify each error term described above. In section 4.1 we derive an expression for $\mathrm{Var}[d_{\mathrm{avg}}]$, the uncertainty in our mean aperture measurement. In section 4.2, to estimate $\langle e^2_{p_{ij}} \rangle$, we derive an expression for $\mathrm{Var}[d_{\mathrm{norm}_{ij}}]$ at each location ij as a function of measured intensities and average this expression over all ij. In section 4.3 we outline a procedure for quantifying mean square accuracy errors. Because $\langle e^2_{a_{ij}} \rangle$ is a function of the fluid used to measure the fracture and the aperture field itself, it is difficult to derive a general expression for it as we have for $\langle e^2_{p_{ij}} \rangle$. Instead, we subtracted an aperture field with a given source of error minimized from an aperture field (for the same fracture) that included the error source, squared the resulting field, and calculated the mean resulting in an estimate of $\langle e^2_{a_{ij}} \rangle$. Finally, in section 4.4 we present a protocol for minimizing and quantifying total measurement errors, and we present a summary of measurement error in the baseline fracture.

4.1. Mean Aperture

To determine d_{avg}, we inject a measured mass of fluid into a dry cell, acquire an image, and analyze the area of the fracture occupied by the fluid using an adaptive thresholding algorithm [*Nicholl and Glass*, 1994] to delineate phases. Then d_{avg} can be expressed by

$$d_{\mathrm{avg}} = M/(\rho P \delta^2) \qquad (15)$$

where M is the mass of fluid injected into the cell, ρ is the density of the fluid, P is the number of pixels occupied by the fluid, and δ is the length of the side of each square pixel. Each of the terms on the right-hand side of (15) has associated error that must be combined to yield an estimate of $\mathrm{Var}[d_{\mathrm{avg}}]$. A first-order perturbation analysis of (15) yields

$$\mathrm{Var}[d_{\mathrm{avg}}] \cong \frac{\hat{M}^2}{\hat{\rho}^2 \hat{P}^4 \hat{\delta}^4} \mathrm{Var}[P] + \frac{2\hat{M}^2}{\hat{\rho}^2 \hat{P}^2 \hat{\delta}^6} \mathrm{Var}[\delta]$$

$$+ \frac{\hat{M}^2}{\hat{\rho}^4 \hat{P}^2 \hat{\delta}^4} \mathrm{Var}[\rho] + \frac{1}{\hat{\rho}^2 \hat{P}^2 \hat{\delta}^4} \mathrm{Var}[M] \qquad (16)$$

which is especially sensitive to measurement errors in δ owing to the δ^2 dependence of d_{avg}. Applying (15) and (16) to our baseline fracture with the measured values of M, ρ, P, and δ and estimates of their variances yields d_{avg} of 0.222 mm and $\mathrm{Var}[d_{\mathrm{avg}}]$ of $\sim 10^{-6}$ mm^2.

Calculating aperture fields using (4) requires normalizing the field by $\langle A_{ij} \rangle$. For $d_{ij} = d_{\mathrm{avg}} d_{\mathrm{norm}_{ij}}$ to be valid, $\langle A_{ij} \rangle$
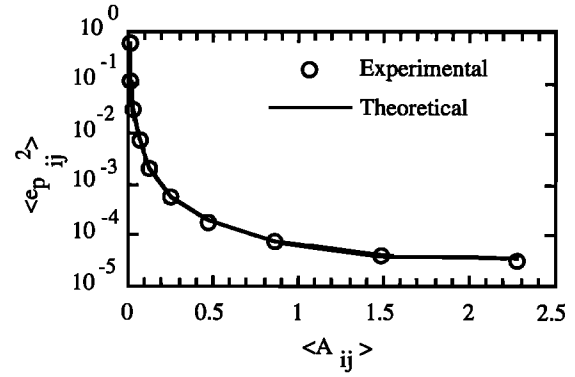
Figure 4. Comparison of theoretical (i.e., equation (18)) and experimentally measured values of $\langle e^2_{p_{ij}} \rangle$ for a range of dye concentrations (Warner Jenkins FD&C Blue #1 dye in deionized water at 1/512, 1/256, 1/128, 1/64, 1/32, 1/16, 1/8, 1/4, 1/2, and 1 g/L).

should be calculated only over the area occupied by the fluid used to measure d_{avg}. The mean aperture of the entire field can then be calculated by averaging the resulting d_{ij} over the entire field.

4.2. Precision Analysis

The combination of noise and spatial variability in the CCD response yields a loss of precision in aperture measurements. Here we quantify how the uncertainties in $\bar{I}_{ij}$ represented by $\mathrm{Var}[\bar{I}_{ij}]$ in (11) result in the mean square precision error $\langle e^2_{p_{ij}} \rangle$. A first-order perturbation analysis of (4) gives

$$\mathrm{Var}[d_{\mathrm{norm}_{ij}}] \cong (\mathrm{Var}[I_{\mathrm{cl}_{ij}}]/E[I_{\mathrm{cl}_{ij}}]^2$$

$$+ \mathrm{Var}[I_{\mathrm{dye}_{ij}}]/E[I_{\mathrm{dye}_{ij}}]^2) \langle A_{ij} \rangle^{-2} \qquad (17)$$

where $I_{\mathrm{cl}_{ij}}$ and $I_{\mathrm{dye}_{ij}}$ are the intensities measured at location ij with clear and dyed solution, respectively. We can estimate $\mathrm{Var}[d_{\mathrm{norm}_{ij}}]$ without measuring it explicitly by approximating $E[I_{\mathrm{cl}_{ij}}]$ and $E[I_{\mathrm{dye}_{ij}}]$ by $\bar{I}_{\mathrm{cl}_{ij}}$ and $\bar{I}_{\mathrm{dye}_{ij}}$ and approximating $\mathrm{Var}[\bar{I}_{\mathrm{cl}_{ij}}]$ and $\mathrm{Var}[\bar{I}_{\mathrm{dye}_{ij}}]$ using (11).

Equation (17) provides an estimate of the variance of $d_{\mathrm{norm}_{ij}}$ at each pixel of the field. We estimate the mean square precision error over the entire field as

$$\langle e^2_{p_{ij}} \rangle \cong \langle \mathrm{Var}[d_{\mathrm{norm}_{ij}}] \rangle \qquad (18)$$

Figure 4 compares experimentally measured values of $\langle e^2_{p_{ij}} \rangle$ to the theoretical results obtained using (18). We see that $\langle e^2_{p_{ij}} \rangle$ can be reduced by increasing the dye concentration used to measure $I_{\mathrm{dye}_{ij}}$, thus increasing $\langle A_{ij} \rangle$.

4.3. Accuracy Analysis

Accuracy or bias error is often quantified by comparing data obtained using a given measurement system to known standards. Unfortunately, constructing a realistic standard for a rough-walled fracture is difficult, and it would have to be measured using some other measurement technique. A cell consisting of two pieces of flat glass separated by accurately measured shims could be used; however, it is difficult to ensure that the glass is perfectly flat and difficult, if not impossible, to predict how the measurement system will respond when a complicated rough surface replaces the smooth glass. Instead, we designed tests to consider the validity of two critical assumptions of the measurement theory as applied in our meth-
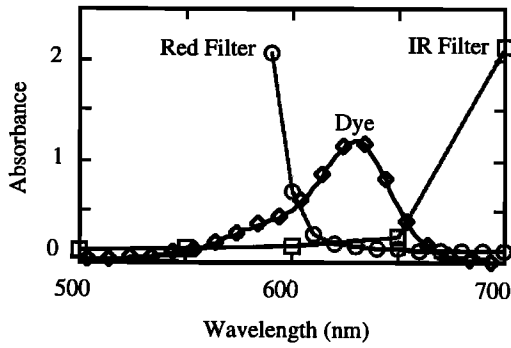
Figure 5. Absorbance spectra of FD&C Blue #1 dye at 0.008 g/L (measured using a two-beam spectrophotometer) and the two camera filters (Kodak Red #25 and Infra Red #301A; absorbance spectra provided by Kodak).

od: (1) the Beer-Lambert law holds for the dye and light source-sensor system and (2) light rays at the fracture walls are not refracted. Deviation from these assumptions leads to increased error. We quantify the total loss of accuracy in our measurements due to these two assumptions as

$$\langle e_{a_{ij}}^2 \rangle = \langle e_{B_{ij}}^2 \rangle + \langle e_{r_{ij}}^2 \rangle + 2 \ \mathrm{Cov} \ [e_B, e_r]_{ij} \qquad (19)$$

where $e_{B_{ij}}$ and $e_{r_{ij}}$ are the errors in $d_{\mathrm{norm}_{ij}}$ due to deviation from the assumptions of the Beer-Lambert law and refraction in the system, respectively. These are bias errors that are constant, for a given location and fluid, regardless of the effects of noise in the measurement system. Though both $e_{B_{ij}}$ and $e_{r_{ij}}$ are controlled by fracture geometry, in the baseline fracture, the covariance of the two error terms is several orders of magnitude smaller than the variances and can be ignored.

4.3.1. Applicability of Beer-Lambert law. The requirement of a monochromatic light source is the primary deviation of our system from the assumptions of the Beer-Lambert law, and we explore this in detail below. In theory, the requirement of monochromatic light can be met by filtering light at the source or at the camera, assuming that frequency shifts due to refraction in the fracture cell are negligible. For our system we use a band-pass filter (combination of Kodak Infra Red filter #301A and Red #25) on the camera lens that is centered on the peak absorbance of the dye (Warner Jenkins FD&C Blue #1). Figure 5 shows the absorbance plotted against wavelength of the dye at one concentration and the two filters used to isolate the optimal wavelength. While this filter combination narrows the bandwidth of measured light to approximately 650 ± 50 nm, it does not satisfy the requirement of a monochromatic light source. Integration over a range of wavelengths typically causes nonlinear absorbance with respect to concentration [*Rossiter and Baetzold*, 1993].

As seen in Figure 5, μ and I_o are both functions of wavelength. Rewriting (2) with $C_1 = 0$, $C_2 = C$, $I_1 = I_{cl}$ and $I_2 = I_{dye}$ and integrating over a range of wavelengths gives

$$I_{dye} = \int_{\gamma_{min}}^{\gamma_{max}} I_{cl}(\gamma) e^{-\mu(\gamma)Cd} \, d\gamma \qquad (20)$$

where γ is the wavelength of the light measured by the CCD and γ_{min} and γ_{max} are the minimum and maximum wavelengths passed by the filter, respectively [*Brodersen*, 1954]. Combining $\mu(\gamma)$ with the intensities transmitted by the filters

(taken directly from Figure 5) as an approximation to $I_{cl}(\gamma)$ and numerically integrating (20) from 600 to 700 nm at different values of C yields a hypothetical relationship between absorbance and concentration for the range of wavelengths measured by our system. Figure 6 compares absorbance versus concentration determined by numerically integrating (20) (nonlinear) and by using the approximate single effective wavelength (linear) at a range of values of d (0.05, 0.1, 0.15, and 0.2 mm). At each value of d, as concentration approaches zero, the slope of the nonlinear function approaches μd, the slope of the linear function. Also, as concentrations increase, the larger aperture measurements show larger relative deviations from the linear function, which indicates that bandwidth integration causes absorbance to become a nonlinear function of d as well as C.

We evaluate the effect of this polychromatic nonlinearity on our measurement system by calculating a series of 10 aperture fields using images of the fracture cell filled with 1/512 g/L through 1 g/L dye solutions. At each concentration, 100 images were acquired, adjusted to correct for temporal fluctuations in the light source, and averaged. The average images were then aligned to the 0 g/L average image with a tolerance of ±0.025 pixels (maximum shift of 0.2 pixels). Applying (4) to each of the 10 concentration fields results in a series of aperture fields that can be directly compared. Plotting the same transect from several of the measured aperture fields demonstrates the effect of integration over γ (i.e., polychromatic source) on aperture measurements (Figure 7). At high concentrations, owing to bandwidth integration, large apertures are smaller and small apertures are larger. At intermediate concentrations, 1/16 g/L and 1/64 g/L, the shape of the aperture field changes little, but the effect of noise becomes noticeable in the 1/64 g/L field. As the concentration is lowered below 1/16 g/L, the decreasing difference between I_{cl} and I_{dye} causes noise to have a significant effect on the normalized aperture field measured using 100 images.

Plotting absorbance versus concentration for measurements at different locations in the fracture representing a wide range
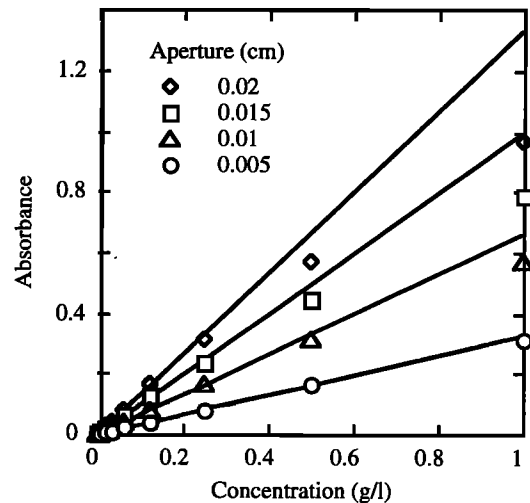
Figure 6. Theoretical comparison of absorbance versus concentration at different d for μ measured at a single wavelength (monochromatic absorbance coefficient: lines) and μ integrated over a range of wavelengths as described by equation (20) (polychromatic absorbance coefficient: points).
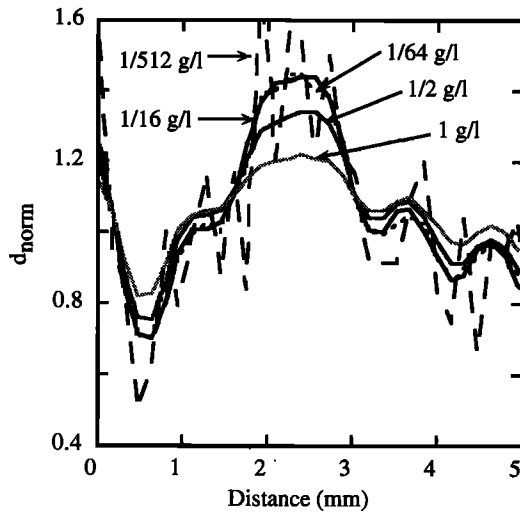
of apertures (Figure 8) shows the same type of nonlinearity we see in Figure 6. For concentrations approaching zero the slope of the curve of absorbance versus concentration approaches the value of μd for the effective single wavelength. To quantify the loss of accuracy as a function of increasing dye concentration for our polychromatic system, we estimate the effective single wavelength slope by fitting the data in Figure 8 with a function of the form

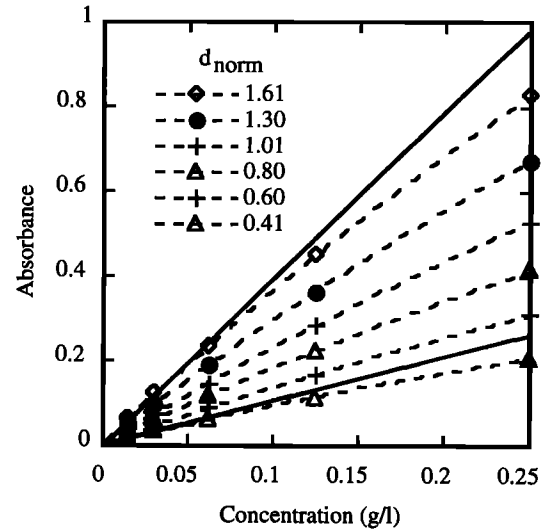$$A = \alpha C/(\beta + C) \tag{21}$$

where α and β are fitting parameters. This function fits our data well for concentrations up to 1/4 g/L and approaches a constant slope of $\mu d = \alpha/\beta$ as C approaches zero. As described by (17), precision error increases not only with decreasing concentration, but with decreasing aperture as well; increased precision error in the measured absorbance at low concentration causes problems fitting (21), especially at small apertures. For this reason, the fields below 1/64 g/L were not used. Using $\alpha_{ij}/\beta_{ij} = \mu d_{ij}$, we calculate a corrected normalized aperture field as

$$d_{\text{norm}_{ij}} = \mu d_{ij}/\langle \mu d \rangle_{ij} \tag{22}$$

Subtracting the corrected aperture field calculated using (22) from each of the 10 aperture fields calculated using (4) gives a measure of error at each pixel of the field as a function of concentration. These errors are a combination of $e_{B_{ij}}$ and $e_{P_{ij}}$. A plot of the RMS error ($\sqrt{\langle e_{B_{ij}}^2 \rangle + \langle e_{P_{ij}}^2 \rangle}$) as a function of concentration is shown in Figure 9. At the optimal concentration of 1/16 g/L the error reaches a minimum near 0.8%. At concentrations >1/16 g/L, integration of $\mu(\gamma)$ over a range of wavelengths causes the error to increase approximately linearly up to the maximum tested concentration of 1 g/L (RMS error $\cong$ 10%). However, smaller signal ranges at concentrations below 1/16 g/L cause dramatic increases in $e_{P_{ij}}$ owing to noise (see Figure 4). We can estimate $\langle e_{B_{ij}}^2 \rangle$ by subtracting $\langle e_{P_{ij}}^2 \rangle$ (as described by (18)) from the RMS error shown in Figure 9. For the 1/16 g/L field, $\sqrt{\langle e_{P_{ij}}^2 \rangle} \cong 0.2\%$, resulting in $\sqrt{\langle e_{B_{ij}}^2 \rangle} \cong 0.8\%$ of the mean. Note that this assumes that $\text{Cov}[e_B, e_P]_{ij} \cong$

Figure 8. Absorbance versus dye concentration at versus locations of the fracture cell having a range of different normalized apertures. The normalized apertures were calculated with $C = 1/16$ g/L. The dashed curves through the data points are the result of fitting equation (21) through each set of points, while the solid lines correspond to the slope at $C = 0$ of these curves for the smallest and largest aperture.

0; this is generally the case for combinations of precision errors (random error at location ij) and accuracy errors (constant error at location ij). The technique presented above for developing a corrected aperture field can be used for routine measurements; however, once the optimal concentration is determined for a fracture, the excessive amount of data generated makes using a single concentration desirable.
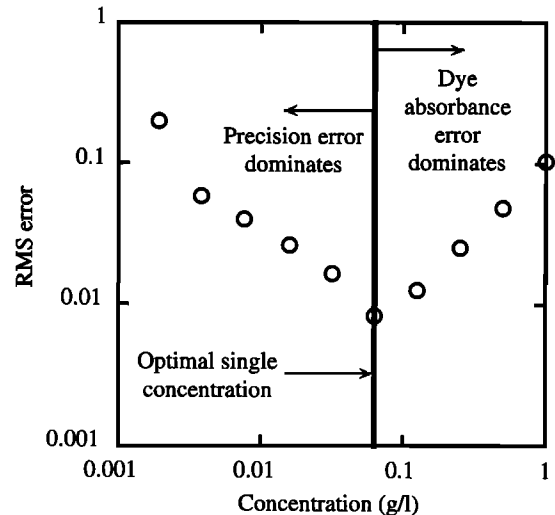

Figure 7. Transects of normalized aperture fields measured using different dye concentrations C. For small C, noise reduces the precision of the transects, while at large C, nonlinearity of dye absorbance causes decreasing accuracy in the transects.

Figure 9. Root-mean-squared (RMS) error in aperture fields as a function of concentration. The RMS error is a combination of precision errors and errors due to nonlinear dye absorbance (i.e., $\sqrt{\langle e_{B_{ij}}^2 \rangle + \langle e_{P_{ij}}^2 \rangle}$). The distinct minimum at $C = 1/16$ g/L indicates the optimal single concentration for measuring aperture fields in the baseline fracture. At lower concentrations, precision errors dominate the total error, while at higher concentrations, the precision errors become insignificant (i.e. Figure 4) and absorbance errors dominate.

Table 1. Estimates of the Root-Mean-Square of Different Error Sources Measured Over a Single Field (% of Mean Aperture)

Precision Errors[a] $\langle e_{P_{ij}}^2 \rangle$	Concentration of FD&C Blue #1, g/L		
	1/16	1/2	1.0
Noise error			
n_{ij}	2.5	0.6	0.6
n_{ij} (50 images)	0.3	0.1	0.1
n_{ij} (100 images)	0.2	0.1	0.1
Shifting error			
$s(0, 0)_{ij}$	0.0	0.0	0.0
$s(0.2, 0.2)_{ij}$	0.7	0.2	0.2
$s(>1, >1)_{ij}$	1.6	0.5	0.5

Accuracy Errors	Concentration of FD&C Blue #1, g/L		
	1/16	1/2	1.0
Dye absorbance error			
$\langle e_{B_{ij}}^2 \rangle$	0.8	4.8	10.4
Refraction error			
$\langle e_{r_{ij}}^2 \rangle$	1.1[b]		~0[c]

Total Error (135% sucrose)	Concentration of FD&C Blue #1, g/L		
	1/16	1/2[d]	1.0[e]
1 image, no shifts	2.6	4.8	10.4
100 images, no shifts	0.9	4.8	10.4
1 image, 0.2 pixel shift	2.7	4.8	10.4
100 images, 0.2 pixel shift	1.2	4.8	10.4

The d_{avg} error for Var[d_{avg}] is 0.5.

[a]Root-mean-square of errors n_{ij} and $s(\Delta i, \Delta j)_{ij}$ represent the error in the normalized aperture field caused by each error term.

[b]For 0.0% sucrose by weight.

[c]For 135.0% sucrose by weight.

[d]Concentration used by *Nicholl and Glass* [1994].

[e]Concentration used by *Glass* [1993].

4.3.2. Effect of refraction on measurements.

The relatively large distance between the CCD camera and the fracture cell (~1.1 m) causes the camera to measure light that crosses the fracture aperture essentially normal to the regional or macroscopic fracture plane. Using a 60-mm lens with the camera height adjusted such that the baseline fracture fills the entire field causes light rays at the ends of the field to leave the fracture at $90° \pm 0.005°$, which results in aperture overestimation with distance from the center of the field. The maximum overestimation is 1.0%, but as this error is controlled by the geometry of the system, it can be removed by applying a correction to the calculated aperture field. However, if refraction occurs at the fluid-glass interface, it is difficult to predict the angle at which light rays have passed through the aperture and hence difficult to determine the magnitude of the resulting measurement errors.

Snell's law describes refraction at an interface between two different media as

$$\eta_1 \sin \theta_1 = \eta_2 \sin \theta_2 \qquad (23)$$

where η_1 and η_2 are the refractive indices of media 1 and 2, respectively, and θ_1 and θ_2 are the respective angles of incidence and refraction measured from a vector normal to the

interface between the two media. Note that refraction at the bottom plate has no effect on our measurements because the bottom plate acts as an additional diffuser plate that is constant for the duration of an experiment. As the interface angle increases from zero, an increasing amount of light is reflected. On the basis of Snell's law, if $(\eta_1/\eta_2) \sin \theta_1 > 1$, then all light is internally reflected and it is impossible to measure aperture at such locations. Reflection of a portion of the transmitted light will not directly affect the measurement because the portion of light reflected will be constant for all images (i.e., independent of dye concentration). The reflection of light at the fluid-glass interface can, however, affect the measurement of the aperture field because reflection increases the probability that stray light will be measured at nearby pixels.

When the refractive indices of the fluid and glass are not matched, refraction at the upper fluid-glass interface results in measurement errors $e_{r_{ij}}$ at each pixel. We evaluate these errors by comparing aperture measurements of the baseline fracture cell made with a sucrose solution to measurements made with deionized water. A 135% by weight sucrose solution ([mass of sucrose]/[mass of solvent]) was used to match the refractive index of the glass. We used dye concentrations of 0 and 1/20 g/L and, to reduce noise in the resulting aperture fields, took a series of 80 images of the fracture filled with each fluid combination. We adjusted each image for temporal fluctuations in the light source, checked for shifts (maximum shift of 0.06 pixels), realigned, and averaged each series of images.

Subtracting the aperture field calculated with the 0% sucrose solution from the 135% solution results in an estimate of $e_{r_{ij}} + e_{P_{ij}}$ at each pixel. We squared this error field, calculated its mean, and subtracted $\langle e_{P_{ij}}^2 \rangle$ (estimated using (18)), resulting in $\sqrt{\langle e_{r_{ij}}^2 \rangle} \cong 1.1\%$. This assumes that $\text{Cov}[e_r, e_p]_{ij} \cong 0$, which, as mentioned in section 4.3.1, is typically the case for combinations of precision and accuracy errors. For our baseline fracture, in which angles of the fracture surfaces are small (normally distributed with a mean of 5.3° and standard deviation of 4.0°), errors due to refraction are small when deionized water is used as the solvent. However, in a fracture with steeper angles relative to the focal plane these errors may become significant. We also note that matching the refractive index of the fluid to that of the glass often alters fluid properties and thus may not be desirable in the context of process experimentation.

4.4. Protocol for Minimizing and Quantifying Measurement Errors

On the basis of our evaluation of different sources of error, it is clear that a procedure designed solely to increase precision will sacrifice accuracy and vice versa. We outline a protocol for systematically balancing precision and accuracy in aperture measurements that is a compilation of the steps taken to estimate individual error sources described in sections 4.1–4.3. As we have described, precision is controlled by spatial and temporal variability of the CCD, while accuracy is specific to the geometry of the fracture being measured. Therefore the dye concentration that minimizes the total error must be determined for each new fracture measured with a given system. This protocol assumes that the precision error inherent to the measurement system has been quantified and provides a procedure for minimizing and quantifying fracture specific errors.

We acquire images with the fracture aperture filled with a series of dye concentrations. Applying (18) to the measured intensities at each concentration provides guidance on the
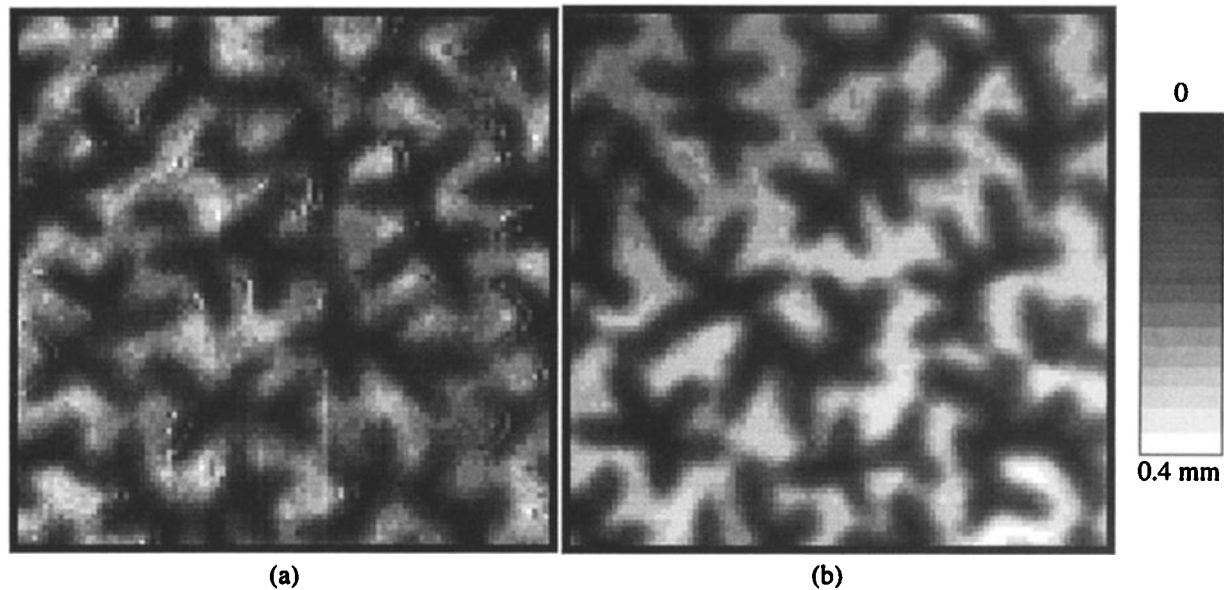
Figure 10. Comparison of similar but nonidentical (10 × 10 mm) glass surfaces measured by (a) laser profilometry (0.1-mm spacing with resolution of 0.007 mm) and (b) light transmission technique (0.1-mm spacing with resolution of 0.009 mm). The discontinuities in the laser profilometry image are features of the measurement method and are not inherent to the glass. The legend refers to twice the profiled elevation (for profilometry field) and aperture (for light transmission field).

number of images to average at each concentration to achieve a desired precision. After acquiring the desired number of images at each concentration, we choose a reference image, adjust each image for temporal fluctuations in the light source, and confirm that Δi, $\Delta j \cong 0$ for each image. This results in a single image for each concentration with known precision.

To quantify dye absorbance error, (4) is applied to the average image at each concentration. These results are compared to corrected images obtained using (22). We then develop a plot similar to Figure 9 and choose the optimal dye concentration which results in the minimum total error. Finally, we evaluate error due to refraction by using a solution that closely matches the refractive index of the fracture walls; if the error is unacceptable, we match the refractive indices of the fluid and fracture walls each time that we measure the aperture field in the fracture. Cell disassembly, cleaning, and reassembly should not influence the choice of solutions and parameters for aperture field measurement or the resulting measurement errors if subsequent fields exhibit a similar aperture distribution to the original field.

Applying the protocol described above to the baseline fracture with results for $\mathrm{Var}[d_{avg}]$ (section 4.1), $\langle e_{p_{ij}}^2 \rangle$ (section 4.2), and $\langle e_{a_{ij}}^2 \rangle$ (section 4.3) yields an estimated total RMS error (i.e., $\sqrt{\langle d_{ij}'^2 \rangle}$) of 0.9% of the mean aperture. As a demonstration of the relative importance of each of the individual sources of error, Table 1 illustrates the magnitude of the different error terms and combines them into several representative values of the total RMS error (expressed as % of mean aperture). For the optimal concentration of 1/16 g/L the measurements are noticeably more sensitive to precision errors; however, averaging 100 images reduces these errors by a factor of 10 (to ~30% of the magnitude of the dye absorbance error). At higher concentrations the dye absorbance error dominates the total error such that the contribution of the other error terms becomes negligible.

5. Comparison to Other Methods

A variety of both destructive and nondestructive methods have been used to measure fracture aperture, including epoxy resin injection with subsequent destructive sectioning [*Gale*, 1987; *Hakami and Larsson*, 1996], surface profilometry [*Brown and Scholz*, 1985; *Cardenas-Garcia and Severson*, 1996], nuclear magnetic resonance imaging [*Kumar et al.*, 1995], and X-ray computed tomography [*Johns et al.*, 1993; *Montemagno and Pyrak-Nolte*, 1995]. The nature of the system required for each method and the sensitivity of the fracture aperture to changes in pressure, confining pressure, temperature, etc., makes it very difficult to directly compare measurements of the same fracture using different techniques. Here we first consider a comparison of light transmission with standard laser profilometry conducted on similar but nonidentical surfaces. We then compare the error determined for light transmission with that of a number of other applied methods reported in the literature.

Glass [1993] reported laser profilometry measurements of a piece of textured glass cut from the same stock as that used to construct the baseline fracture. Figure 10 compares light transmission measurements from the surface of a piece of this textured glass (mated with flat glass) to the piece measured using laser profilometry. The laser profilometer had a beam diameter of 0.007 mm with data measured at 0.1 mm increments. To obtain comparable data with the light transmission technique, we measured a ~20 × 20 mm zone of the glass at a spatial resolution of 0.009 mm (estimated RMS error = 1.1%); a grid with 0.1-mm spacing was removed to yield a data set similar to the profilometry measurements. Figure 10 shows irregularities and discontinuities in the profilometry measurements that are not present in the light transmission measurements. Inspecting the glass under a microscope indicates that these irregularities are not inherent to the glass. An additional difficulty with using profilometry to measure fracture apertures

is that it is necessary to profile both surfaces and mate them numerically [e.g., Brown, 1987]. For studies of flow and transport in fractures this numerical step makes it very difficult to obtain an aperture field that is identical to the actual fracture in which experiments are performed.

Table 2 presents a comparison of the current light transmission results to previously reported methods, including an earlier application of light transmission [Nicholl and Glass, 1994]. The evaluation of error for each of the methods was approximated by statements made in the papers and may not reflect the full capabilities of the methods if a detailed evaluation of error such as performed here were accomplished; however, we see that the RMS error (% of mean) for the current light transmission study is much lower than that determined from the other methods. Additionally, the spatial resolution of the measurements is higher, and the number of measurements is ~3 orders of magnitude greater. The spatial resolution is dictated primarily by the optics of the system and by the array size of the CCD. Finally, we note that only X-ray and nmr can provide aperture field measurements nondestructively at the time of the experiment as can the light transmission method.

6. Influence of Measurement Error on Simulated Flow and Transport

To illustrate the influence of measurement error in the aperture field on hypothesized experimental results, we simulate flow and transport in the baseline fracture under saturated and partially saturated conditions with models that are currently presumed to embody the appropriate underlying physics. For simplicity, we consider only accuracy errors in $d_{norm_{ij}}$ that are representative of earlier studies reported in the literature. Previous authors, applying light transmission methods to measure aperture fields, used higher dye concentrations than optimal to increase the contrast between small- and large-aperture regions [e.g., Nicholl and Glass, 1994; Persoff and Pruess, 1995]. Nicholl and Glass [1994] observed that the distribution of the resulting aperture field they measured using 1/2 g/L dye solution was narrower than an aperture field generated by numerically mating laser profilometry measurements of a single surface of the same glass. To reconcile this difference, they stretched the distribution of their measured field by scaling each individual measurement appropriately to yield a minimum aperture of ~0 and a maximum of approximately twice the mean value as exhibited by the mated profilometry data. Thus we generated aperture fields with representative error by using a dye concentration of 1/2 g/L (narrow field), then scaled the distribution of the 1/2 g/L aperture field (wide field) as was done by Nicholl and Glass [1994]. Figure 11 compares the aperture distribution of these two fields to the aperture field generated using a dye concentration of 1/16 g/L (optimal field), and Figure 7 compares transects from the narrow and optimal fields. The same mean aperture (0.0222 cm) was applied to each field, but the variances of the distributions differ as a result of the accuracy errors associated with each field. The fields were 12.7 × 28.0 cm (800 × 1764 pixels), and we estimated the RMS errors to be 0.9, 4.8, and 12.2% for the optimal, narrow, and wide fields, respectively.

We applied a finite difference solution to the Reynolds equation [e.g., Brown, 1987] to simulate saturated flow through each field. The simulated transmissivities of the narrow (0.080 cm²/s) and wide (0.072 cm²/s) fields relative to the optimal field (0.078 cm²/s) were ~103.1 and 92.5%, respectively. We next

Table 2. Comparison of Resolution, Mean Aperture, and Associated Error in Aperture Measurement Techniques Reported in Literature

Technique	Type of Fracture	Data Source	Mean Aperture, mm	RMS Error, % of mean	Resolution, mm	Size of Fracture, cm × cm	Number of Measurements
Light transmission (nondestructive)	Analog baseline fracture	present study	0.222	0.9	0.16 × 0.16	15.2 × 30.4	1.81E + 06
	Single textured surface mated with flat glass	present study	0.121	1.1	0.009 × 0.009	1.8 × 1.8	4.00E + 06
	Analog baseline fracture[a]	Nicholl and Glass [1994]	0.215	8.6[b] 4.8[c]	0.14 × 0.14	15.2 × 30.4	1.81E + 06
	Induced fracture in a limestone core[d]	Kumar et al. [1995]	0.265	11.4[e]	0.31 × 0.31	5.1 × 6.9	3.66E + 04
Nuclear magnetic resonance imaging (nondestructive)	Natural fractures in two granite cores:						
Computerized X-ray tomography (nondestructive)	Core A	Johns et al. [1993]	0.25–0.50[f]	12.5[g]	1.465 × 1.465 × 5.0	5.7 × 14.6	~1.1E + 03
	Core C, fracture L		0.20–0.25[f]	12.5[g]	0.7325 × 0.7325 × 5.0	8.2 × 24.0	~5.4E + 03
Epoxy injection/sectioning (destructive)	Natural fracture in a granite core	Hakami and Larsson [1996]	0.360	2.8–8.4[h]	0.2 × ~10[i]	19.0 × 41.0	~3.0E + 04

Read 1.81E + 06 as 1.81 × 10⁵.
[a]This was a different fracture than the baseline fracture used in the current study made out of similar pieces of glass.
[b]Measurement error was not reported by investigators but was quantified using their technique to calculate an aperture field with the data from the current study. Their technique involved stretching the distribution of the measured field to match the distribution of a field created by numerically combining laser profilometry measurements of a single surface to yield an aperture field. The distribution of this artificially created aperture field is wider than the distribution determined using the current method.
[c]This error was calculated using the current technique with the dye concentration and sucrose concentration used by the previous investigators.
[d]Also measured fracture in a granite core; however, the magnetic nature of granite caused significant measurement errors.
[e]RMS error term is a combination of bias error determined by measuring a limestone calibration phantom with known aperture (5.1%) and NMRI precision error (10.2%).
[f]Mean aperture varied over length of core.
[g]Reported ± 0.05-mm fluctuations of measurement of a 0.4-mm granite phantom.
[h]Based on reported accuracy of 10–30 μm.
[i]Aperture measured at 0.2-mm intervals along slices cut perpendicular to fracture plane; the distance between each slice was ~10 mm.
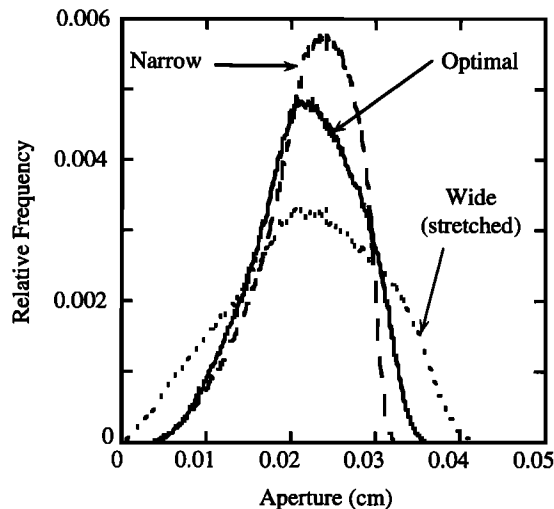
Figure 11. Baseline fracture aperture distributions for fields calculated using 1/16 g/L (optimal), 1/2 g/L (narrow), and a third field calculated by stretching the 1/2 g/L aperture distribution (wide) to closely match the distribution of a field generated by numerically mating two surfaces measured using laser profilometry.

used a two-dimensional random-walk particle-tracking algorithm to simulate solute transport through the saturated flow fields [e.g., *Moreno et al.*, 1998]. Particle displacements in each time step consisted of an advective displacement based on local velocities calculated using the pressure field from the Reynolds equation solution and a random diffusive displacement. The particles were initially placed along a line of constant concentration 0.4 cm from the narrow inflow edge of the fracture, and breakthrough curves (BTCs) were determined as the particles left the fracture. The BTCs were all approximately Gaussian, indicating a Fickian dispersion process. Because all three simulations were run under the same gradient, the earliest arrival time for each fracture reflected the difference in the transmissivities. However, the dispersivities, which are independent of the small differences in mean velocity, show significant deviations from that measured for the optimal field (0.025 cm). In the narrow field, smaller variability in the aperture field caused a reduction in the dispersivity to 0.021 cm (~84% of the optimal), while in the wide field the dispersivity increased to 0.083 cm (~332% of the optimal). These results demonstrate the significant sensitivity of dispersion estimates to aperture measurements due to the fact that the local velocities controlling dispersion are a function of d_{ij}^2.

As an example of the influence of aperture field error on flow and transport under partially saturated conditions, we considered flow through a wetting water phase with a residual entrapped nonwetting air phase. The entrapped structure was simulated with a modified invasion percolation model [*Glass et al.*, 1998] by invading an initially air-filled fracture with water from the narrow inflow edge (no flow conditions along the long edges, and air can escape out the edge opposite water invasion) until all apertures are filled with either water or entrapped air. Figure 12 shows representative portions of the simulated phase structures from each aperture field. In addition to the differences in saturations of the narrow (0.77) and wide (0.62) fields relative to the optimal field (0.67) of ~114 and 93%, the character of the entrapped clusters is noticeably different.
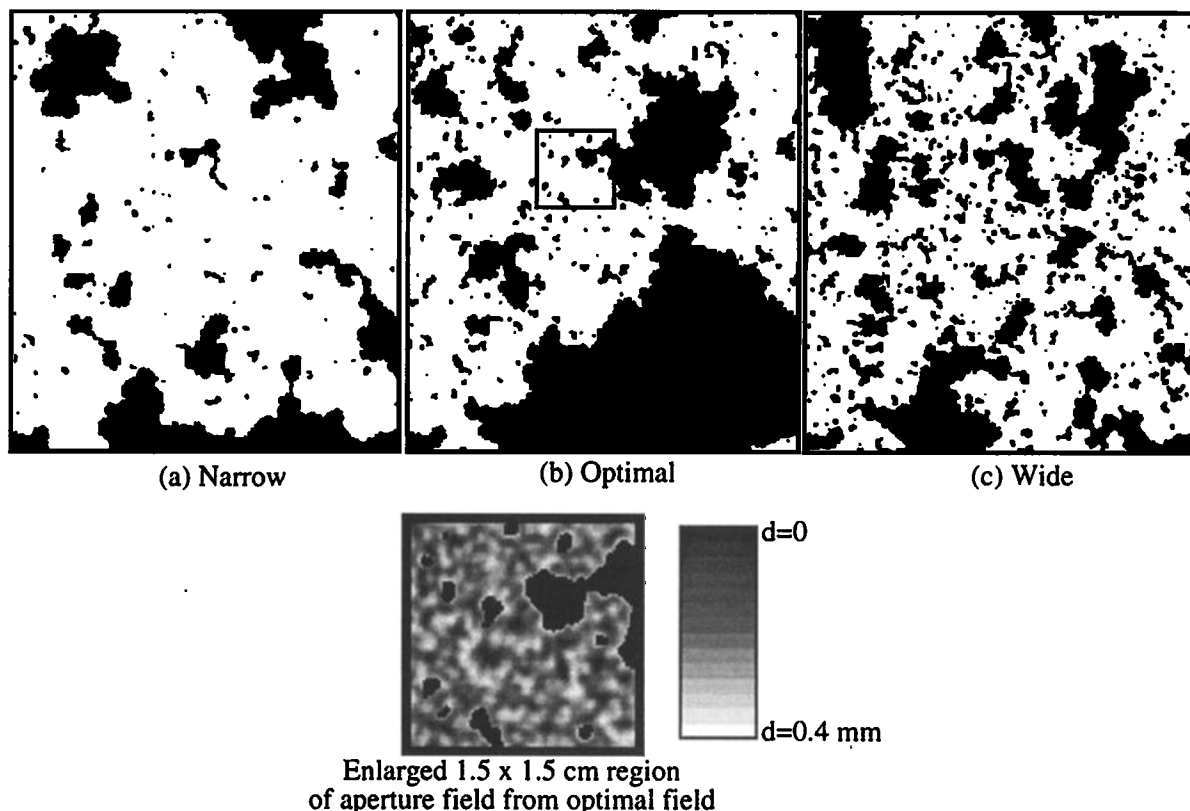
These features have a significant influence on flow and transport and compound the errors in simulations for the saturated condition. The simulated transmissivities through the partially saturated narrow (0.035 cm^2/s) and wide (0.018 cm^2/s) fields relative to the optimal field (0.021 cm^2/s) were ~167 and 85%, respectively. For solute transport the influence of channeling caused by the entrapped air can be seen in the BTCs as multiple peaks (Figure 13), each corresponding to a channel through the corresponding field, thus defying a Fickian interpretation and quantitative comparison of dispersivities. Qualitatively, we find that while each of these fields has similar large-scale entrapped structures, the number of medium- and small-scale structures increased from the narrow field to the wide field, causing increased mixing between secondary channels. This increased mixing dampens the influence of channeling, resulting in a decrease in the number of independent peaks in the BTCs from the narrow field to the wide field.

This simple demonstration illustrates the different sensitivities of models and model combinations (hypothesized experimental results) to accuracy-based aperture field error representative of earlier work. We note that since the mean aperture is the same in each field, these errors modify only the variance of the aperture field. Of course, precision-based errors and errors in the measured mean aperture will also influence model results, possibly each in a different way. If not characterized, errors and compounded error such as we see under partially saturated conditions can lead to extreme difficulties in the testing of conceptual and numerical models. If error cannot be ascribed to the aperture field, then deviations between model and experiment cannot be properly evaluated. If error cannot be minimized beyond a level required to distinguish two conceptual models, then one model cannot be chosen over the other. Thus the combination of experimental observations and model simulations to further understand flow and transport in fractures requires careful consideration of aperture field measurement and the technique applied to obtain it.

7. Conclusion

We have evaluated and improved a light transmission method to measure aperture fields in transparent fractures and characterize the associated error. This technique yields known, minimized error, high-resolution, nondestructive measurements that can be made at the time of an experiment. Therefore the measured aperture field is matched to measurements of phase structure and/or solute (dye) concentration at any location within the fracture during a two-phase or transport experiment, making the system ideal for studying the physics of processes where void space geometry has a critical control. For natural fractures where a transparent cast can be fabricated [e.g., *Hakami and Barton*, 1991; *Persoff and Pruess*, 1995; *Wan et al.*, submitted manuscript, 1999], the light transmission method can be applied not only in the context of process experimentation but also as a characterization tool for natural fracture aperture fields.

It has been shown that increasing dye concentration causes accuracy error to increase while precision error decreases, and an optimal concentration can be obtained that yields the lowest error for a given fracture. Minimized error measurements of the baseline fracture made with our current system have estimated RMS errors of 0.9% (0.002 mm) of the mean aperture (0.222 mm). This method results in significantly lower error than other techniques reported in the literature. The general

(a) Narrow   (b) Optimal   (c) Wide

d=0

d=0.4 mm

Enlarged 1.5 x 1.5 cm region
of aperture field from optimal field

Figure 12. Representative ~8 × 8 cm portions of the 12.7 × 28 cm field for (a) narrow (1/2 g/L), (b) optimal (1/16 g/L), and (c) wide (1/2 g/L stretched) aperture fields showing wetting phase (white) and residual entrapped nonwetting phase (black) structure simulated with a modified invasion percolation model. As the aperture distribution widens, the complications of the entrapped structure and the number of small- and medium-scale clusters increases.

approach for minimizing and evaluating error presented here can be used directly to improve other full field measurement techniques based on energy transmission such as those used in micromodels [e.g., *Wan et al.*, 1996; *Corapcioglu et al.*, 1997],
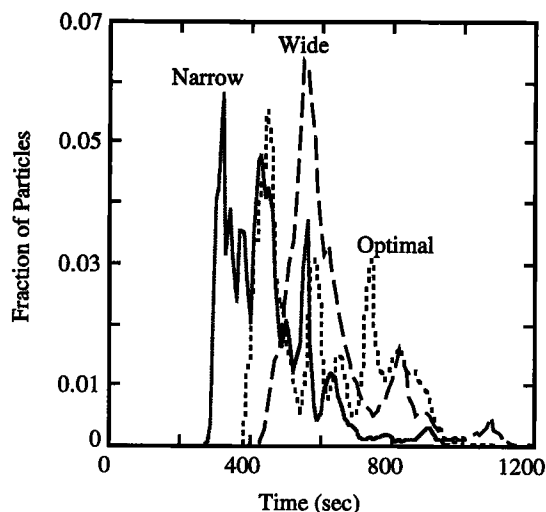
Figure 13. Breakthrough curves for the transport simulations through the partially saturated aperture fields. The number of independent peaks in the breakthrough curves is significantly influenced by the entrapped phase structure in each field.

Hele-Shaw cells [e.g., *Cooper et al.*, 1997], and thin porous systems [e.g., *Norton and Glass*, 1993; *Tidwell and Glass*, 1994; *McBride and Miller*, 1994].

Simulations of flow and transport through fracture aperture fields with ~10% RMS error, typical of that reported in the literature to date, demonstrate the importance of fully characterizing and minimizing error in aperture field measurements. We find that model results for single-phase flow (Reynolds equation), transport (particle tracking), phase structure (modified invasion percolation), and their various combinations for two-phase flow and transport have significantly different sensitivities to the aperture field and thus force different requirements for its measurement. Appropriate experimental tests of numerically implemented theory must be designed with these requirements in mind.

version of the paper [Detwiler et al., 1999] with additional detail on the measurements that support our results and the derivation of the linear perturbation results (equations (16) and (17)) can be obtained from the authors.

References

Brodersen, S., Slit-width effects, J. Opt. Soc. Am., 44, 22-25, 1954.

Brown, S. R., Fluid flow through rock joints: The effect of surface roughness, J. Geophys. Res., 92, 1337-1347, 1987.

Brown, S. R., and C. H. Scholz, Broad bandwidth study of the topography of natural rock surfaces, J. Geophys. Res., 90, 12,575-12,582, 1985.

Brown, S. R., A. Ciprihan, and R. Hardy, Experimental observations of fluid flow channels in a single fracture, J. Geophys. Res., 103, 5125-5132, 1998.

Cardenas-Garcia, J. F., and G. R. Severson, Optical, noncontact, automated experimental techniques for three-dimensional reconstruction of object surfaces using projection moire, stereo imaging, and phase-measuring profilometry, U.S. Geol. Surv., Rep. 95-433, 1996.

Cooper, C. A., R. J. Glass, and S. W. Tyler, Experimental investigation of the stability boundary for double-diffusive finger convection in a Hele-Shaw cell, Water Resour. Res., 33, 517-526, 1997.

Corapcioglu, M. Y., S. Chowdhury, and S. E. Roosevelt, Micromodel visualization and quantification of solute transport in porous media, Water Resour. Res., 33, 2547-2558, 1997.

Detwiler, R. L., S. E. Pringle, and R. J. Glass, Aperture field measurement in transparent rough walled fractures using two-dimensional full field light transmission, Rep. SAND99-1134, Sandia Natl. Lab., Albuquerque, N. M., 1999.

Gale, J. E., Comparison of coupled fracture deformation and fluid flow models with direct measurements of fracture pore structure and stress-flow properties, in Proceedings of the 28th U.S. Symposium on Rock Mechanics, pp. 1213-1222, A. A. Balkema, Brookfield, Vt., 1987.

Geller, J. T., S. E. Borglin, and B. Faybishenko, Experimental study and evaluation of dripping water in fracture models, Eos Trans. AGU, 79(45), Fall Meet. Suppl., F383, 1998.

Gentier, S., D. Billaux, and L. van Vliet, Laboratory testing of the voids of a fracture, Rock Mech. Rock Eng., 22, 149-157, 1989.

Glass, R. J., Modeling gravity-driven fingering in rough-walled fractures using modified percolation theory, paper presented at 4th International Conference of High Level Radioactive Waste Management, Am. Nucl. Soc., April 26-30, Las Vegas, Nev., 1993.

Glass, R. J., and M. J. Nicholl, Quantitative visualization of entrapped phase dissolution within a horizontal flowing fracture, Geophys. Res. Lett., 22, 1457-1460, 1995.

Glass, R. J., and V. C. Tidwell, Research program to develop and validate conceptual models for flow and transport through unsaturated, fractured rock, paper presented at 2nd International Conference of High Level Radioactive Waste Management, Am. Nucl. Soc., Las Vegas, Nev., April 28 to May 3, 1991.

Glass, R. J., M. J. Nicholl, and M. E. Thompson, Comparison of measured and calculated permeability for a saturated, rough-walled fracture, Eos Trans. AGU, 72(44), Fall Meet. Suppl., 216, 1991.

Glass, R. J., M. J. Nicholl, and L. Yarrington, A modified invasion percolation model for low-capillary number immiscible displacements in horizontal rough-walled fractures: Influence of local in-plane curvature. Water Resour. Res., 34, 3215-3235, 1998.

Hakami, E., and N. Barton, Aperture measurements and flow experiments using transparent replicas, Publ. Norges Geotek. Inst., 182, 1-8, 1991.

Hakami, E., and E. Larsson, Aperture measurements and flow exper-

iments on a single natural fracture, Int. J. Rock Mech. Min. Sci. Geomech. Abstr., 33, 395-404, 1996.

Johns, R. A., J. S. Steude, L. M. Castanier, and P. V. Roberts, Nondestructive measurements of fracture aperture in crystalline rock cores using X ray computed tomography, J. Geophys. Res., 98, 1889-1900, 1993.

Kneafsey, T. J., and K. Pruess, Laboratory experiments on heat-driven two-phase flows in natural and artificial rock fractures, Water Resour. Res., 34, 3349-3367, 1998.

Kumar, A. T. A., P. D. Majors, and W. R. Rossen, Measurement of aperture and multiphase flow in fractures using NMR imaging, paper presented at SPE Annual Technical Conference and Exhibition, Soc. of Pet. Eng., Dallas, Tex., Oct. 22-25, 1995.

McBride, J. F., and C. T. Miller, Optimization of phase-fraction measurements using single- and dual-photon-energy attenuation, Eos Trans. AGU, 75(16), Spring Meet. Suppl., 148, 1994.

Montemagno, C. D., and L. J. Pyrak-Nolte, Porosity of natural fracture networks, Geophys. Res. Lett., 22, 1397-1400, 1995.

Moreno, L., Y. W. Tsang, C. F. Tsang, F. V. Hale, and I. Neretnieks, Flow and tracer transport in single fracture: A stochastic model and its relation to some field observations, Water Resour. Res., 24, 2033-2048, 1988.

Nicholl, M. J., and R. J. Glass, Wetting phase permeability in a partially saturated horizontal fracture, paper presented at 5th International Conference of High Level Radioactive Waste Management, Am. Nucl. Soc., May 22-26, Las Vegas, Nev., 1994.

Nicholl, M. J., R. J. Glass, and H. A. Nguyen, Gravity-driven fingering in unsaturated fractures, paper presented at 3rd International Conference of High Level Radioactive Waste Management, Am. Nucl. Soc., April 12-16, Las Vegas, Nev., 1992.

Nicholl, M. J., R. J. Glass, and S. W. Wheatcraft, Gravity-driven infiltration instability in initially dry nonhorizontal fractures, Water Resour. Res., 30, 2533-2546, 1994.

Norton, D., and R. J. Glass, Full-field dye concentration measurement within saturated/unsaturated thin slabs of porous media, paper presented at 4th International Conference of High Level Waste Management, Am. Nucl. Soc., April 26-30, Las Vegas, Nev., 1993.

Persoff, P., and K. Pruess, Two-phase flow visualization and relative permeability measurement in natural rough-walled rock fractures, Water Resour. Res., 31, 1175-1186, 1995.

Rossiter, B. W., and R. C. Baetzold, Physical Methods of Chemistry: Determination of Electronic and Optical Properties, John Wiley, New York, 1993.

Russ, J. C., The Image Processing Handbook, CRC Press, Boca Raton, Fla., 1992.

Su, G., J. Geller, K. Pruess, J. Hunt, and M. Dragilia, Features of preferential flow paths in heterogeneous, unsaturated fractures, Eos Trans. AGU, 79(45), Fall Meet. Suppl., F383-F384, 1998.

Tidwell, V. C., and R. J. Glass, X-ray and visible light transmission for laboratory measurement of two-dimensional saturation fields in thin slab systems, Water Resour. Res., 30, 2873-2882, 1994.

Wan, J., T. K. Tokunaga, C.-F. Tsang, and G. S. Bodvarsson, Improved glass micromodel methods for studies of flow and transport in fractured porous media, Water Resour. Res., 32, 1955-1964, 1996.

R. L. Detwiler, Department of Civil, Environmental, and Architectural Engineering, University of Colorado, Boulder, CO 80302.

R. J. Glass and S. E. Pringle, Flow Visualization and Processes Laboratory, Sandia National Laboratories, Geohydrology Department 6115, MS 0175, Albuquerque, NM 87115-0735. (rjglass@sandia.gov)